



HAL
open science

Wall-pressure fluctuations of laminar separation bubble based on direct numerical simulation and experiments over a hydrofoil at $Re = 450,000$

Antoine Ducoin, J.A. Astolfi

► **To cite this version:**

Antoine Ducoin, J.A. Astolfi. Wall-pressure fluctuations of laminar separation bubble based on direct numerical simulation and experiments over a hydrofoil at $Re = 450,000$. *European Journal of Mechanics - B/Fluids*, 2019, 76, pp.132-144. 10.1016/j.euromechflu.2019.02.001 . hal-02877142

HAL Id: hal-02877142

<https://hal.science/hal-02877142v1>

Submitted on 22 Oct 2021

HAL is a multi-disciplinary open access archive for the deposit and dissemination of scientific research documents, whether they are published or not. The documents may come from teaching and research institutions in France or abroad, or from public or private research centers.

L'archive ouverte pluridisciplinaire **HAL**, est destinée au dépôt et à la diffusion de documents scientifiques de niveau recherche, publiés ou non, émanant des établissements d'enseignement et de recherche français ou étrangers, des laboratoires publics ou privés.



Distributed under a Creative Commons Attribution - NonCommercial 4.0 International License

1 Wall-pressure fluctuations of Laminar Separation
2 Bubble based on Direct Numerical Simulation and
3 Experiments over a Hydrofoil at $Re=450,000$

4 A. Ducoin^a, J. A. Astolfi^b

5 ^a *LHEEA laboratory, Ecole Centrale de Nantes (CNRS UMR 6598), 44300 Nantes,*
6 *France*

7 ^b *Institut de Recherche de l'Ecole Navale EA 3634, Ecole Navale, 29240 Brest Cedex 9,*
8 *France*

9 **Abstract**

10 The objective of this paper is to investigate wall-pressure fluctuations
11 downstream of a Laminar Separation Bubble (LSB) on a laminar NACA66
12 hydrofoil section, based on Direct Numerical Simulation (DNS) and exper-
13 imental analysis. DNS is performed using the massively parallelized open
14 source code NEK5000, which uses the high order spectral element method
15 to solve the incompressible Navier-Stokes equations. It is compared to mea-
16 surements performed in a hydrodynamic tunnel at the French Naval Academy
17 Research Institute (IRENav). A Reynolds numbers of $Re = 450,000$ with
18 an angle of attack of $\alpha = 4^\circ$ is considered, which induces an LSB to the rear
19 of the maximum thickness of the boundary layer. The local wall pressures
20 at three different locations are compared: just downstream of the LSB at
21 $x/c=0.7$, in the breakdown region of the LSB at $x/c=0.8$ and in the fully
22 turbulent region at $x/c=0.9$. The DNS results compare very well with the
23 measured wall pressures. The DNS captures efficiently the periodic fluctu-
24 ations downstream of the LSB, up to the random behavior induced by the

*corresponding author
Preprint submitted to *European Journal of Mechanics - B/Fluids* December 27, 2018
antoine.ducoin@ec-nantes.fr

25 transition to turbulence. Analysis of the boundary layer flow obtained by
26 DNS suggests that an H-type or K-type transition occurs, characterized by
27 2D TS waves and typical Λ structures, that break down and generate tur-
28 bulence. Moreover, it shows that intense and localized pressure fluctuations
29 occur in the breakdown region.

30 *Key words:* laminar separation bubble, wall pressure fluctuation,
31 transition, laminar propeller section, spectral element method

32 **1. Introduction**

33 For many marine applications operating at low angles of attack, laminar
34 profiles can be chosen for the propeller blade in order to reduce friction at
35 the body surface and hence improve performance. However, this leads to
36 development of further transitional regimes, even at high Reynolds numbers
37 where the boundary layer is usually considered to be fully turbulent. These
38 transitional regimes can induce large pressure fluctuations and hence wide
39 variation in the hydrodynamic loadings. Hence, numerical and experimental
40 investigations are still necessary to help predict performance in the context of
41 marine propeller sizing. Moreover, the present study can help to improve the
42 physical understanding of (i) cavitation inception at the blade surface, which
43 is known to occur inside Laminar Separation Bubbles (LSB) in the case of
44 transitional flows, and (ii) laminar separation-induced structural vibrations.

45

46 Typically, this type of transition occurs at low to moderate Reynolds num-
47 bers and is triggered by a laminar separation and a reversed flow, caused by
48 an adverse pressure gradient. The development of the turbulent flow induces

49 a momentum transfer in the direction normal to the wall, which reattaches
50 the flow. An LSB or transitional separation bubble is then generated ([16]),
51 which is characterized by a dead region near the laminar separation, and an
52 unstable region near the reattachment point. This point is usually subjected
53 to a low frequency oscillation in the shear layer (known as *flapping*), which
54 is responsible for the first destabilization of the LSB. Meanwhile, it has been
55 shown that primary instabilities (Kelvin-Helmholtz vortex and/or Tollmien-
56 Schlichting waves) lead to LSB vortex shedding. Upstream of the LSB, the
57 flow is highly unstable and is governed by complex mechanisms identified as
58 primary and secondary instabilities that lead to transition to turbulence.

59

60 The physical understanding of laminar to turbulent transition over lift-
61 ing profiles is derived primarily from aerodynamic applications on small-scale
62 devices, where the transition comprises a large portion of the chord and dom-
63 inates the boundary layer flow. The associated Reynolds numbers are typi-
64 cally in the range $20,000 < Re < 100,000$. In order to study the transition to
65 turbulence at these high Reynolds numbers, DNS studies of transitional flows
66 were introduced approximately a decade ago, supported by experimental ob-
67 servations. It has been shown both experimentally [17] and numerically [22]
68 that the transitional region appears near the trailing edge for low to mod-
69 erate angles of attack, and moves towards the leading edge as the angle of
70 attack increases. The transition on the SD7003 geometry has been exten-
71 sively investigated for Reynolds numbers in the range $20000 < Re < 66000$,
72 and for different angles of attack using experimental [3, 40, 30, 29] and nu-
73 merical methods [39, 38]. At $Re = 20000$, transition is observed near the

74 trailing edge and a vortex associated with a Kelvin-Helmholtz instability is
75 convected into the foil's wake, which strongly interacts with the well-known
76 von Kármán instability. In [13], the characteristic frequency of LSB vortex
77 shedding matches the Strouhal number found in the work of [33], defined for
78 a flat plate with a pressure gradient. For $Re = 66000$, transition is stronger
79 and a burst phenomenon is associated with a fast transition to turbulence
80 [3, 39], although Kelvin-Helmholtz instabilities may still be observed. Jones
81 et al. [21] performed a numerical analysis of an LSB in the case of an airfoil at
82 $\alpha = 5^\circ$ with a low Reynolds number, $Re = 50000$. The authors investigated
83 the instability mechanisms leading to the breakdown to turbulence, linking
84 the breakdown to the combination of two absolute instabilities: an elliptic
85 instability and a mode-B or hyperbolic instability. An important conclusion
86 was that, in the absence of a convectively driven transition effect within the
87 shear layer, an absolute instability can take place, weakening the influence of
88 free stream turbulence. More recently, an interesting DNS study investigated
89 the effect of aspect ratio on laminar to turbulent transition on a NACA0012
90 profile ([41]). Due to computational costs, the simulation used a reduced
91 span and periodic boundary conditions. The results suggest that different
92 aspect ratios result in close predictions of the time-averaged aerodynamic
93 quantities, although small aspect ratios tend to under-predict the turbulent
94 fluctuations near the separation point but over-predict them inside the sep-
95 aration bubble. This work highlighted the importance of setting span length
96 correctly to predict the development of turbulence. However, the effect of
97 aspect ratio on the initial development of coherent structures downstream
98 from the LSB has not been investigated.

99 The NACA4412 airfoil profile has also been extensively investigated, mainly
100 for wind turbine applications. In the experiments of [26], the location and
101 formation of LSB were affected both by Reynolds number (ranging from
102 $Re = 25,000$ to $Re = 50,000$) and angle of attack. Moreover, the near wake
103 seems to be affected by LSB and trailing-edge separation, as also observed
104 by [13]. This profile has been also investigated numerically for aircraft appli-
105 cations involving a much higher Reynolds number, $Re = 400,000$ [19]. The
106 authors use the spectral element code NEK5000, and set over 3.2 billion grid
107 points, with an element order of 12 and a full domain. This work showed
108 the ability of the spectral element method to predict the transition and the
109 development of turbulence. The authors also showed that adverse pressure
110 gradients have a great influence on the development of the boundary layer
111 and turbulent kinetic energy.

112

113 As far as hydrodynamic applications are concerned, very few papers have
114 addressed the prediction of transitional flows on marine propellers. Those
115 that do usually use RANS based codes with empirical transition models, and
116 hence no LSB dynamic is captured. In [2], the authors show that the use of
117 a transition model leads to an improvement in the flow pattern and slight
118 increases in thrust. However, prediction of the transition location is strongly
119 dependent on the values for turbulence inlet used by the model. [34] investi-
120 gated how application of a transition model influences the flow prediction for a
121 cavitating marine propeller. The results clearly correlated cavitation incep-
122 tion with the location of transitional regions, however, conclusions could not
123 be drawn concerning the influence of transition modeling on cavitation de-

124 velopment and global propeller performance. Similar conclusions are drawn
125 in [14]. More academically, experimental studies on LSB have been carried
126 out on marine propeller sections (i.e. hydrofoils) at the Naval Academy Re-
127 search Institute (IRENav), France. Several of these studies concerned the
128 NACA66 section, for which highly transitional flows have been observed for
129 relatively high Reynolds numbers ($Re=300,000$ to $1,000,000$). It has been
130 shown that a very strong and localized transition to turbulence occurs inside
131 the boundary layer, which induces intense pressure fluctuations ([11]) that
132 strongly influence hydrodynamic performance [8]. Moreover, it has been
133 demonstrated that this type of transition induces important structural vi-
134 brations. [12] showed that there could be a strong interaction between these
135 vibrations and the physics of LSB vortex shedding. In particular, additional
136 frequencies close to that of LSB shedding and structural modes were observed
137 in the vibration spectra in transitional flows, as well as a global increase in
138 amplitude, which could be the result of a complex fluid structure interac-
139 tion phenomenon. This work also showed that when the frequency of LSB
140 vortex shedding approaches a natural vibration mode, resonance with the
141 natural frequencies of the blade can be obtained and additional harmonics
142 of the main LSB shedding frequency are observed. It should be noted that
143 this behaviour is quite different from that of transition-induced vibrations on
144 membrane wings, which is a major field of investigation of transition-induced
145 vibration. The latter case is characterized by much lower Reynolds numbers
146 and large deformations of the structure, which is seen to significantly change
147 the LSB characteristics [9]. Moreover, the laminar profiles of a marine pro-
148 peller are obtained by moving the maximum thickness to the center of the

149 chord, which reduces the adverse pressure gradient and hence increases the
150 critical Reynolds number of transition, Re_θ , see Figure 1. This results in a
151 delay of transition compared with conventional, non-laminar profiles, and a
152 modification of the Re_θ slope after transition occurs, which can induce dif-
153 ferent physical processes compared to existing aerodynamic studies.

154

155 Finally, although a link between LSBs and cavitation inception has been
156 clearly identified by John Carlton in his book about marine propellers [5],
157 it remains poorly understood. It is known that the effect of LSB strongly
158 depends on the scale of the propeller, its surface roughness and the nuclei den-
159 sity. For a model scale with low surface roughness, the position of cavitation
160 inception is related to the transition point, i.e. the location of the LSB. For
161 high angles of attack (before stall), cavitation germs may be trapped inside
162 the LSB to form cavitation patches at the leading edge. Further develop-
163 ment of these patches typically results in sheet cavitation. In [1], the authors
164 studied cavitation on a two-dimensional Eppler hydrofoil. They found some
165 indication of the presence of a separation bubble through pressure measure-
166 ments. At the suction side, a region with a near-constant pressure aft of the
167 pressure peak was observed, and cavitation inception is observed as a band
168 along the leading edge, similar to the type of inception associated with lam-
169 inar separation. Moreover, examination of the spanwise vorticity indicates a
170 thin region of vorticity production which could be an additional indicator of
171 the presence of a thin leading edge flow separation, where cavitation appears.

172

173 For lower angles of attack, the LSB is located from the mid-chord up to the

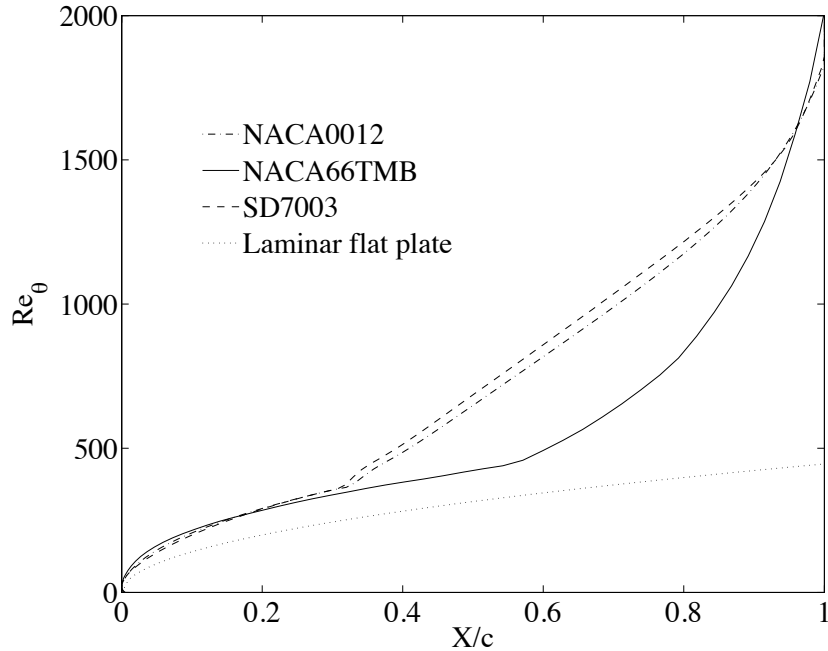


Figure 1: Critical Reynolds number Re_θ along the chord obtained with Xfoil. Comparison of laminar (NACA66) and non-laminar (NACA0012 and sd7003) profiles at $Re = 450,000$.

174 trailing edge, depending on the inflow conditions and hydrofoil geometry, and
 175 cavitation typically occurs in this region, which is mainly correlated with the
 176 adverse pressure gradient and the location of minimum pressure. Because
 177 there is no negative pressure peak, bubbles can grow and form cavitation
 178 bubbles, which appear quite randomly around the minimum pressure at the
 179 surface. As a consequence, further studies investigating the link between
 180 LSB, wall pressure and cavitation are essential.

181

182 Therefore, the objective of the present work is to characterize the wall
 183 pressure downstream from an LSB on a laminar NACA66 section operat-

184 ing at a low angle of attack and at $Re = 450,000$, through a combination
185 of numerical and experimental analysis. Because of the moderate Reynolds
186 number considered, a simplified DNS domain is used and RANS velocity pro-
187 files are implemented for the inflow conditions. A mesh sensitivity analysis
188 was first carried out at a lower Reynolds number ($Re = 225,000$), and a
189 similar resolution is used for the target Reynolds number ($Re = 450,000$) by
190 increasing the elements order. To check the validity of the model, mean flow
191 is compared with the RANS calculation. Then, the wall pressure fluctua-
192 tions are investigated both experimentally and numerically at three different
193 locations between the LSB and the fully turbulent boundary layer. Finally,
194 the flow is analyzed numerically, and conclusions are drawn concerning the
195 particularity of bubble dynamics and its effects on wall pressure fluctuations
196 over laminar hydrofoil sections.

197

198 **2. Experimental method**

199 Measurements were carried out in the cavitation tunnel at IRENav, France.
200 The test section was 1 m long with a $h = 0.192$ m square section. The ve-
201 locity ranged between 0 and 15m/s and the pressure from 30 mbar to 3bars.
202 The hydrofoil was a NACA 66 with a NACA a=0.8 camber type, a camber
203 ratio of 2% and a relative thickness of 12% [27]. It was mounted horizon-
204 tally in the tunnel test section. The chord was $c = 0.150$ m and the span is
205 $b = 0.191$ m, yielding a low aspect ratio $b/c = 1.3$ and a confinement param-
206 eter $h/c = 1.28$. Flow visualizations show that about 80 to 90% of the foil
207 surface could be considered to be 2D flow ([27]), depending on the angle of

208 incidence.

209 Pressure measurements were carried out using seventeen piezo-resistive
210 transducers (Keller AG 2 MI PAA100-075-010) of 10 bars maximum pres-
211 sure. The pressure transducers were mounted into small cavities with a 0.5
212 mm diameter pinhole at the hydrofoil surface. The wall pressure spectrum
213 measured by the transducer was attenuated at the theoretical cut-off fre-
214 quency $f_c = 9152\text{Hz}$. Experiments used a sample frequency of $f = 20\text{kHz}$. A
215 main set of ten transducers was aligned along the chord on the suction side
216 at mid-span, where the flow was considered to be quasi-2D: from the leading
217 edge, at the reduced coordinate $x/c = 0.1$, to the trailing edge, at coordinate
218 $x/c = 0.90$, with a step of $0.10c$.

219 Measurements were performed using an angle of attack $\alpha = 4^\circ$ and upstream
220 velocities ranging from $U_\infty = 1.5\text{ m/s}$ to 10m/s , corresponding to Reynolds
221 numbers ranging from $Re = 225,000$ to $1,500,000$. Under these conditions,
222 laminar flow was maintained over about 60% to 80% of the chord and hence
223 pressure fluctuations were observed starting at $x/c = 0.7$. It was also ob-
224 served that the signal to noise ratio leads to accurate measurements of the
225 physical pressure fluctuations for $U_\infty \geq 3\text{ m/s}$, i.e. $Re \geq 450,000$.

226

227 **3. Computational methods**

228 *3.1. Direct Numerical Simulation*

229 The dynamics of a three-dimensional incompressible flow of a Newtonian
230 fluid are described by the Navier-Stokes equations:

$$\dot{\mathbf{U}} = -(\mathbf{U} \cdot \nabla)\mathbf{U} - \nabla P + Re^{-1}\Delta\mathbf{U} \tag{1}$$

$$\nabla \cdot \mathbf{U} = 0$$

231 where $\mathbf{U} = (U_x, U_y, U_z)^T$ is the velocity vector and P the pressure term.
232 The Reynolds number is defined by $Re = U_\infty c/\nu$, where ν is the kinematic
233 viscosity of the considered fluid, c is the chord length and U_∞ is the upstream
234 velocity.

235 The Navier-Stokes equations were solved using the flow solver NEK5000
236 developed at Argonne National Laboratory by Fischer et al. [15]. The method
237 is based on the spectral elements method (SEM), introduced by Patera [32],
238 which provides spectral accuracy in space while allowing for the geometrical
239 flexibility of finite element methods. Spatial discretization is obtained by
240 decomposing the physical domain into spectral elements within which the
241 velocity is defined on Gauss-Lobatto-Legendre (GLL) nodes and the pres-
242 sure field on Gauss-Legendre (GL) nodes. The solution to the Navier-Stokes
243 equations is then approximated within each element as a sum of Lagrange
244 interpolants defined by an orthogonal basis of Legendre polynomials up to
245 degree N . The results presented in this paper were obtained with a poly-
246 nomial order from $N = 8$ to $N = 12$. The convective terms were advanced
247 in time using an extrapolation of order 3, whereas the viscous terms used a

248 backward differentiation, also of order 3, resulting in the time-advancement
249 scheme labeled BDF3/EXT3. NEK5000 employs the MPI standard for par-
250 allelism [36, 37]. For further details about the spectral element method, the
251 reader is referred to the books by [10] and [24]. The calculations were per-
252 formed on the French National Server named Institute for Development and
253 Resources in Intensive Scientific Computing (IDRIS). IBM Blue Gene/Q was
254 the super computer used, which has high energy efficiency of 2.17 Gflops/W.
255 The main characteristics of this machine include six racks, each having 1024
256 nodes and a total of 98,304 cores with 1GB per core.

257 The scalability of NEK5000 was tested with the present case up to 32768
258 processors and 326 million grid points, and compared with a combustion
259 case with the same code, using a blue Gene/P ([25]), see Figure 2. The re-
260 sults show a large decrease in computing efficiency when the ratio between
261 the number of grid points N and the number of processors P decreases be-
262 low 20000. To achieve an efficiency greater than 90%, the following number
263 of processors were chosen for the simulations: $P = 16384$ at order $O(12)$,
264 $P = 8192$ at order $O(10)$ and $P = 2048$ at order $O(8)$.

265 3.2. Numerical setup

266 Because of the moderate Reynolds number considered for DNS ($Re =$
267 450,000), the DNS domain was restricted to the near wall region, and veloc-
268 ity boundary conditions were imposed at the domain inlet boundaries (left,
269 top and bottom regions) from a transitional RANS calculation to reproduce
270 the velocity gradient external to the hydrofoil boundary layer, see Figure 3.
271 $\nabla \mathbf{U} \cdot \mathbf{x} = 0$ was set at the outlet, whereas a no-slip condition was imposed on
272 the wing surface. Periodic boundary conditions were imposed on the vertical

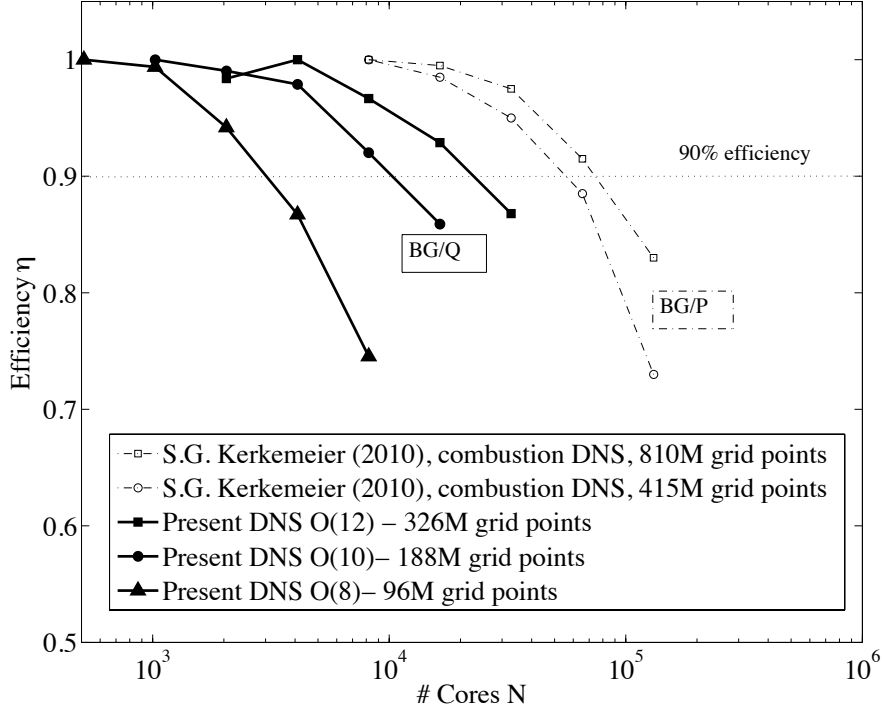


Figure 2: Scalability tests of NEK5000 as function of number of grid points

273 side planes of the domain. The total height of the DNS domain was $0.25c$,
 274 with $0.5c$ in the wake. The span was reduced to $0.05c$. The domain of the
 275 RANS calculation corresponds to the dimensions of the experimental test
 276 section of the hydrodynamic tunnel at IRENav.

277

278 The spectral mesh was determined using the following method: hav-
 279 ing restricted the domain to the near wall region, the spatial resolution
 280 was determined using the wall friction from the RANS calculations, ac-
 281 cording to the general requirements for a DNS at $Re = 450,000$, namely

282 $\Delta y_{min} < 0.2, \Delta x_{max} = \Delta z_{max} < 10$. Then, the span length was set accord-
 283 ing to the computational time allocated for the project, i.e. $0.05c$. It is
 284 important to point out that the reduced span can force development of 3D
 285 boundary layer flow in the transition region, related to the development of
 286 "hairpin structures". Although the influence of Reynolds number on the
 287 transverse wavelength has not been fully characterized in the literature, a
 288 direct dependence has been shown in the experiments of [4] on a sd7003 air-
 289 foil. They show first that LSB thickness linearly depends on boundary layer
 290 thickness. They also show that the transverse wavelength of what they call
 291 C-shape structures is approximately $0.2c$ at $Re = 20,000$, compared to about
 292 $0.1c$ at $Re = 60,000$. It is then reasonable to estimate that this parameter
 293 may be proportional to the boundary layer thickness in the proximity of the
 294 LSB, i.e a laminar boundary layer thickness, which is proportional to $1/\sqrt{Re}$.
 295 Using the current Reynolds number of $Re = 450,000$, this gives an estima-
 296 tion of about $0.04c$ for the transverse wavelength of hairpin structures, so
 297 $0.05c$ was considered a minimum for the present study.

298 The spectral mesh is shown in figure 4. It is refined close to the wall to
 299 obtain a low y^+ value, whereas it is almost constant in the x (chordwise) and
 300 z (spanwise) directions. This leads to 188480 spectral elements, leading to
 301 approximately $O(8)$ at $Re = 225,000$ (mesh sensivity analysis) and $O(12)$ at
 302 $Re = 450,000$ (study case).

303 To obtain the DNS, a progressive increase of the element order was performed
 304 to advance in time, up to the target mesh. As the DNS code is semi-implicit,
 305 it requires the local CFL number to be strictly $CFL = u\Delta t/\Delta x < 0.75$.
 306 The computations were carried out with $CFL \approx 0.5$.

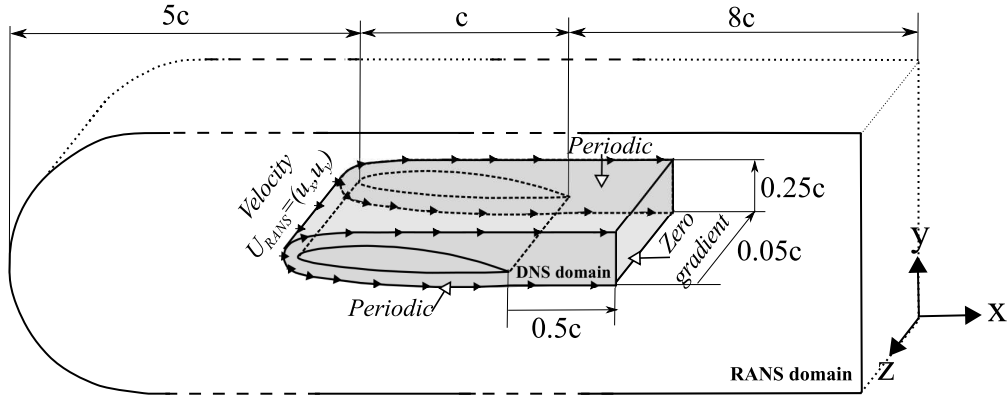


Figure 3: Computational domain of the NACA66 hydrofoil.

307

308 3.3. Isotropic von Kármán turbulence model

309 In order to add the perturbation at the inlet of the computational do-
 310 main, an isotropic von Kármán turbulence model ([23]) was implemented
 311 into the NEK5000 code. This model is based on the energy spectra of the
 312 perturbations. The energy spectrum is set numerically by using random
 313 number-generating algorithms [31] to generate random angles, resulting in a
 314 randomized field. The von Kármán isotropic turbulence model considers the
 315 linear velocity and the angular velocity components of the disturbances as
 316 spatially varying stochastic processes and specifies power spectral density to
 317 each of them.

318 For this study, a modified von Kármán spectrum was utilized:

$$E(\kappa) = c_E \frac{u_{rms}^2}{\kappa_e} \frac{(\kappa_1/\kappa_e)^4}{[1 + (\kappa_1/\kappa_e)^2]^{17/6}} e^{-2(\kappa_1/\kappa_e)^2} \quad (2)$$

319 Here, $\kappa_1 = (\kappa_i \kappa_i)^{1/2}$ and $\kappa_\eta = \epsilon^{1/4} \nu^{-3/4}$ are obtained from the kinetic energy

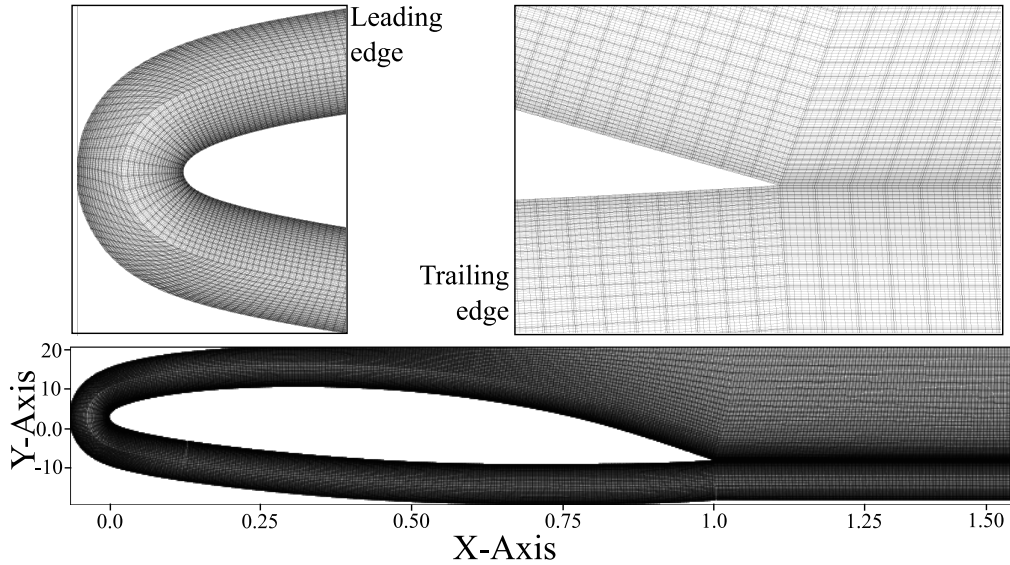


Figure 4: Spectral element mesh of the NACA66 hydrofoil, $N = 188,480$.

320 by integrating the energy spectrum over all the wave numbers, and then
 321 utilizing the gamma functions. κ_e is linked to the smallest wave number, and
 322 c_E is a constant. The mathematical details and derivations can be found in
 323 [18], and details about the von Kármán spectra used here can be found in
 324 [7].

325 The von Kármán model is applied only to a portion of the inlet domain
 326 but covers the entire hydrofoil boundary layer. The disturbances are con-
 327 vected downstream by the free-stream flow, destabilizing the boundary layer
 328 and triggering the turbulence. The integral length scale is set to $0.006c$, cor-
 329 responding to 50% of the boundary layer thickness in the transition region,
 330 whereas the smallest scale corresponds to the smallest cell at the inlet, i.e.
 331 $0.0018c$.

332 *3.4. Sensitivity analysis*

333 A sensitivity analysis was performed for a lower Reynolds number ($Re =$
334 $225,000$) for element orders from $O(6)$ to $O(10)$. The effect of mesh res-
335 olution was investigated in the unsteady region of the LSB where vortex
336 shedding occurs, and in the turbulent region. After selecting the required
337 resolution, the element order was increased to simulate the higher Reynolds
338 number ($Re = 450,000$), assuming that the LSB dynamics would be similar.

339

340 First, the flow in the transition region was analyzed. Figure 5 shows the
341 instantaneous velocity field in the unsteady region of the LSB. **Although**
342 **the figures cannot be directly compared, since they were taken at different**
343 **instants with different mesh resolutions, their prediction of the LSB shed-**
344 **ding process can be qualitatively compared.** The lower order mesh ($O(6)$) is
345 clearly too coarse to capture the LSB vortex shedding correctly. Numerical
346 instabilities disturb the unsteady region of the LSB, resulting in the for-
347 mation of smaller structures, and hence further numerical instabilities form
348 downstream. From order $O(8)$, this numerical effect seems to be suppressed
349 and the shedding process is correctly captured.

350 This observation is confirmed in Figure 6(a), which shows the pressure
351 spectra downstream from the LSB. Due to numerical instabilities, the $O(6)$
352 produces a pressure peak at 125 Hz compared to 85 Hz for $O(8)$ and $O(10)$.
353 The effect of mesh resolution on the development of turbulence is also ob-
354 served near the trailing edge. The spectra of streamwise velocity V_X clearly
355 shows that increasing element order tends to capture a larger range of tur-
356 bulent scales, as indicated by the frequency range over which the slope is

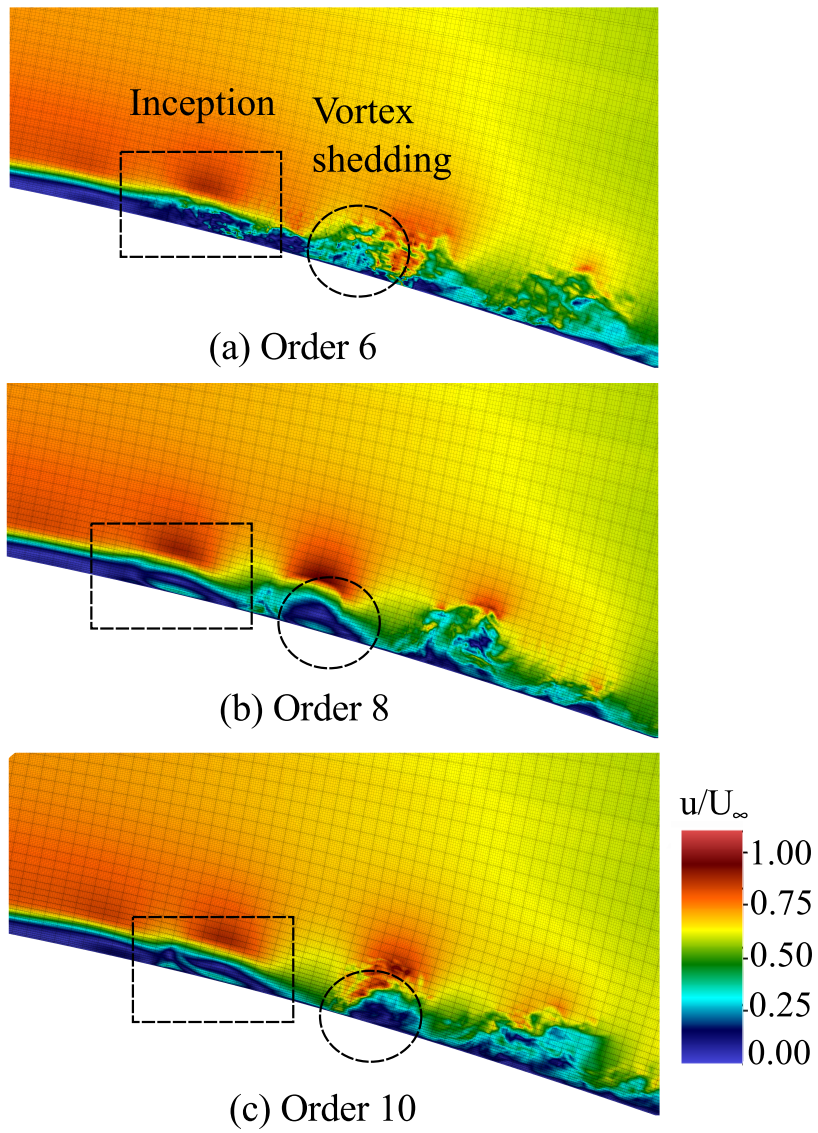


Figure 5: Convergence of the LSB shedding. Velocity contours downstream of the LSB for three different element orders, $Re = 225000$.

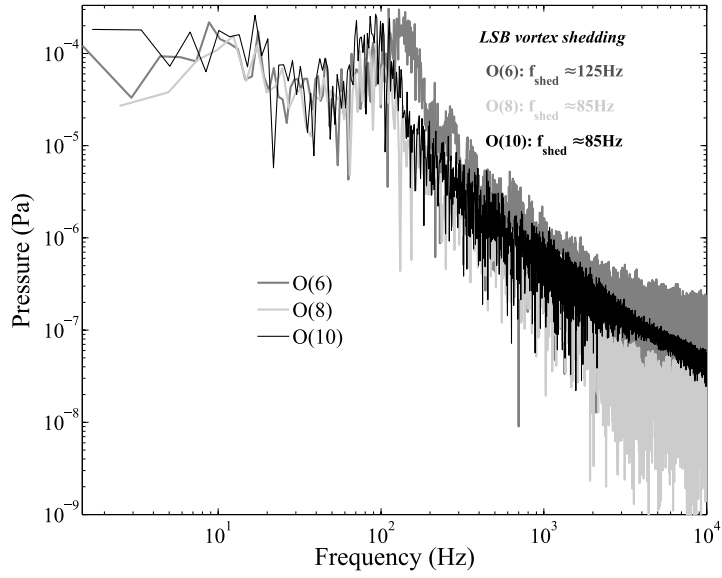
Element order	C_L	C_D
O(6)	0.8198 ± 0.055	0.0213 ± 0.0049
O(8)	0.8272 ± 0.061	0.0219 ± 0.0034
O(10)	0.8274 ± 0.062	0.0215 ± 0.00057

Table 1: Convergence of lift and drag coefficients as a function of the element order, $Re = 225000$.

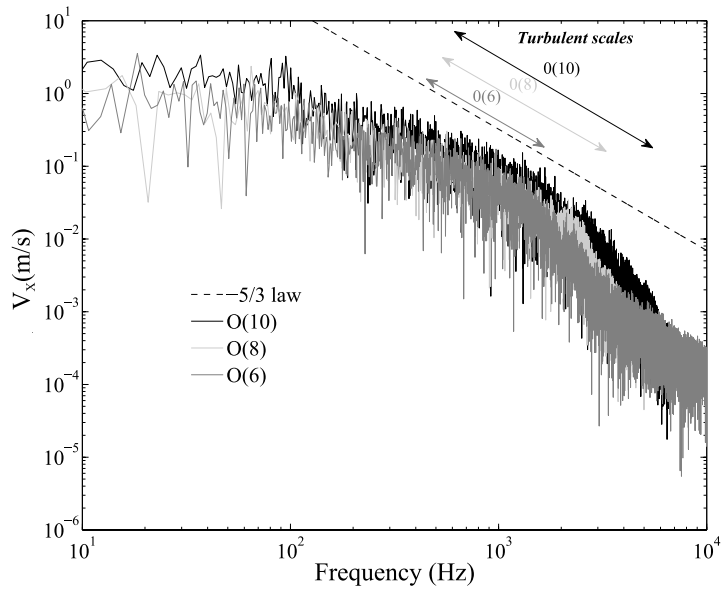
357 $-5/3$, corresponding to the characteristic slope of turbulent cascade. Since
358 the primary objective of the present paper is to investigate LSB dynamics,
359 it is not necessary to achieve convergence on the turbulent spectra.

360 Finally, the effect of element order on components of hydrofoil perfor-
361 mance was tested, see Table 1. It was observed that drag converged for all
362 mesh resolutions, whereas lift is slightly under-predicted for the lower order
363 O(6) mesh, as compared to the O(10) mesh.

364 According to this convergence study, at $Re = 225,000$ the mesh with order
365 O(8) is sufficient to fully capture the LSB dynamics, and the transition to
366 turbulence. The total number of points was $N = 96,501,760$. The element
367 order was then increased to 12 to simulate the case at $Re = 450,000$. Fig-
368 ure 7 shows the final mesh resolution along the chord for the two Reynolds
369 numbers at the wall in the tangential, normal and spanwise directions, re-
370 spectively. It is taken from the friction velocity, which is time and spanwise
371 averaged. Because of the non-uniform distribution of the spectral nodes,
372 Δx^+ and Δz^+ present maximum and minimum values, which are taken from
373 the largest and smallest cells within one spectral element. This corresponds
374 to the maximum resolution as it is at the wall, and because the spectral ele-



(a) Pressure spectra at $x/c = 0.8$



(b) Spectra of V_x at $x/c = 1.0$

Figure 6: Effect of element order on (a) LSB vortex shedding and (b) turbulent scales, $Re = 225000$.

375 ments are uniformly distributed through the domain along the x and z axes.
 376 The final resolution for O(8), $Re = 225000$ leads to $\Delta x_{max}^+ = \Delta z_{max}^+ = 3$
 377 and $\Delta y_{min}^+ = 0.1$, and for O(12) it is $\Delta x_{max}^+ = \Delta z_{max}^+ \approx 7$ and $\Delta y_{min}^+ = 0.2$,
 378 corresponding to 326 million grid points at $Re = 450000$. Even though the
 379 mesh resolution is lower for the higher Reynolds number, it is considered to
 380 be sufficient for analyzing the transitional flow. As a comparison, a similar
 381 method was recently presented in [19] for a DNS around a wing section at a
 382 similar Reynolds number ($Re = 400,000$), using Nek5000 on a NACA4412
 383 over a full domain. This study obtained 3.2 billion grid points with strong
 384 wall refinements, to obtain approximately the same mesh resolution.

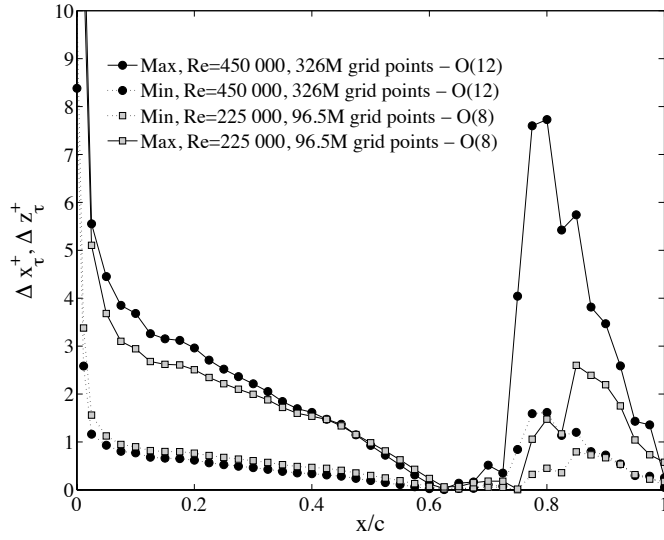
385 4. Results and discussion

386 4.1. Mean flow analysis: DNS at $Re=450,000$

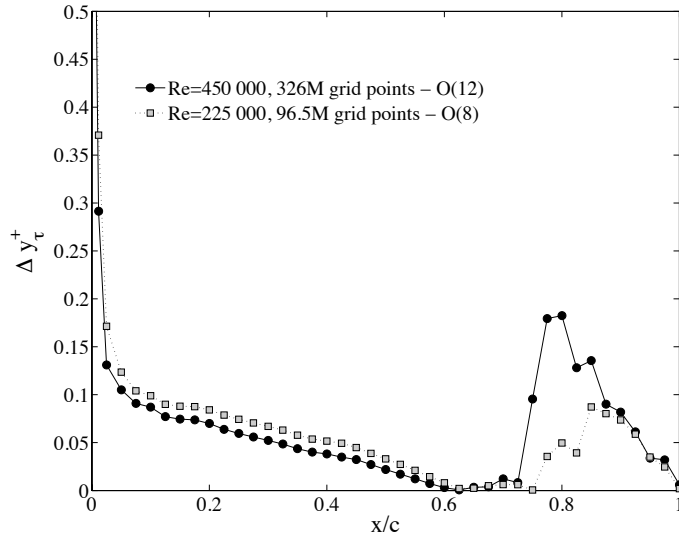
387 To check the validity of the RANS velocity boundary conditions of the
 388 DNS domain, the mean flow obtained with DNS was compared to the tran-
 389 sitional RANS calculations. The velocity fields are shown in Figure 8. Good
 390 agreement is observed overall. **The stagnation at $x/c = 0.0055$ is correctly**
 391 **predicted by DNS, and the velocity gradient is reproduced in the DNS up to**
 392 **the LSB, after which point differences are observed because the RANS solver**
 393 **does not capture the LSB unsteadiness.**

394

395 Local velocity profiles along the chord are shown in Figure 9. Good agree-
 396 ment is observed within the boundary layer; however the DNS calculates
 397 higher external velocities (by approximately 5%) compared to the RANS
 398 calculation, due to added confinement. This numerical error is corrected in



(a) Streamwise (x-axis) and spanwise (z-axis) directions



(b) wall normal direction (y-axis)

Figure 7: Mesh resolution at the hydrofoil surface for the two cases considered

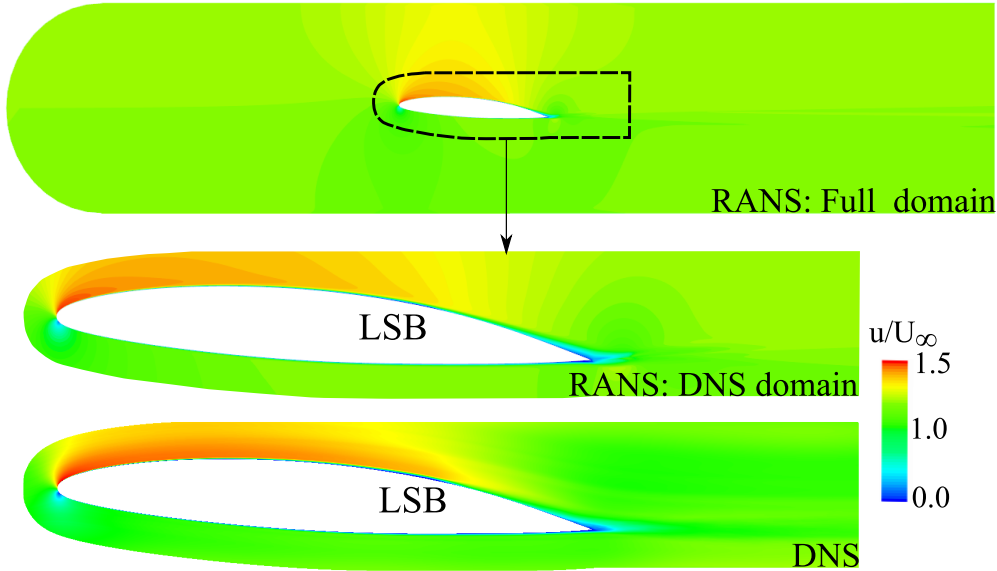


Figure 8: Comparison of the RANS and DNS velocity fields, $Re=450,000$.

399 the results section, to ensure that the pressure coefficient calculations and
 400 the shedding frequencies compare with experimental values. As expected,
 401 the velocities are the same at the upper boundary as RANS velocity profiles
 402 are imposed in the DNS calculations.

403

404 The method was tested for the lower Reynolds number case at $Re=225,000$,
 405 which was used for the sensitivity analysis. As shown in Figure 10, the DNS
 406 calculation of external boundary layer velocities was greater than for the
 407 higher Reynolds number, at 8%. This difference is attributed to the increase
 408 in boundary layer thickness, which magnifies the confinement effects.

409 Table 2 compares the LSB characteristics between RANS and DNS. Since
 410 DNS captures the velocity gradient well, its calculation of laminar separation

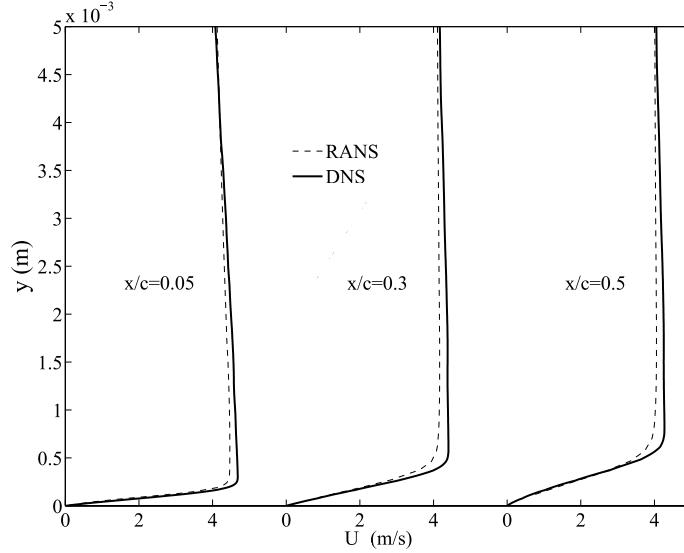


Figure 9: Comparison of the RANS and DNS velocity profiles for three different locations, $Re=450,000$.

411 is very close to the RANS value. It can be seen that the LSB vortex shedding
 412 frequency obtained from DNS (f_{shed}) compares well with the experimental
 413 value ($f_{exp-shed}$) extracted from wall pressure measurements. This is consis-
 414 tent with the work of [33], which used the Strouhal number, $St_\theta = \frac{f_{shed}\theta_{sep}}{u_{sep}}$,
 415 to characterize the shedding frequency, considering it to be dependent only
 416 on the boundary layer quantities at the laminar separation, captured nu-
 417 merically by DNS. The computed Strouhal number is $St_\theta = 0.0090$ for
 418 $Re = 450,000$, as compared to $St_\theta = 0.0068$ found by [33]. This differ-
 419 ence is attributed to the different case studied by [33], namely a flat plate
 420 submitted to a pressure gradient.

421

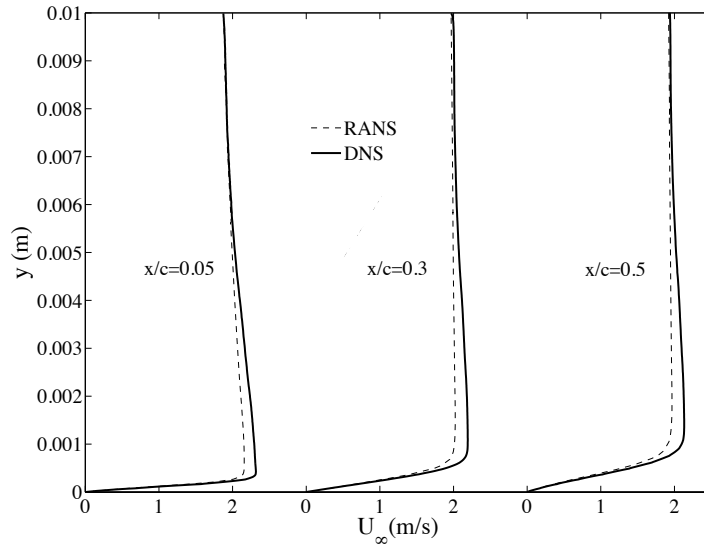


Figure 10: Comparison of the RANS and DNS velocity profiles for three different locations, $Re=225,000$.

Case	x_{sep}	x_{re}	$f_{shed}(\text{Hz})$	$f_{exp-shed}(\text{Hz})$
DNS - $Re=450,000$	0.62	0.72	335	300
RANS - $Re=450,000$	0.65	0.72	-	-

Table 2: Comparison of RANS and DNS LSB characteristics. x_{sep} and x_{re} are the laminar separation and turbulent reattachment location, $f_{shed}(\text{Hz})$ and $f_{exp-shed}$ are the numerical and experimental shedding frequencies.

422 4.2. Investigation of pressure fluctuations: experiments vs DNS at $Re =$
423 450,000

424 Experiments in the cavitation tunnel were first performed at $\alpha = 4^\circ$ for
425 $U_\infty = 1.5$ m/s to 10 m/s in steps of 0.5m/s. The results are shown in Figure
426 11, where frequency spectra of wall pressure at $x/c = 0.7$ and $x/c = 0.8$ are
427 plotted for all the velocities considered. To illustrate the evolution of wall
428 pressure fluctuations with the LSB dynamics, Figure 12 shows the average
429 position of the LSB (in blue), the region of LSB vortex shedding where peri-
430 odic fluctuation occurs (in green), and the fully turbulent region (in red), as
431 the upstream velocity increases.

432 First, it is observed that the frequency of LSB shedding increases linearly as
433 Reynolds number (i.e. U_∞) increases, from about 100 Hz for $U_\infty = 1.5$ m/s,
434 up to about 1000 Hz for $U_\infty = 7$ m/s. **The evolution of this frequency from**
435 **$x/c = 0.8$ to $x/c = 0.7$ visible in Figure 11 illustrates the displacement of the**
436 **LSB along the leading edge.** The frequency peak vanishes after $U_\infty > 3.5$ m/s
437 at $x/c = 0.8$ (Figure 11 (b)) and appears starting $U_\infty > 4$ m/s at $x/c = 0.7$
438 (Figure 11 (a)), which clearly means that periodic fluctuation due to LSB
439 shedding move toward the leading edge. Figure 12 illustrates that this vari-
440 ation (in green) is primarily due to the decrease in LSB size ($U_\infty < 4$ m/s
441 to 4 m/s $< U_\infty < 8$ m/s), which is due to an increase in Reynolds number.
442 Secondly, a decrease in viscous effects slightly increases the adverse pressure
443 gradient, which tends to shift the LSB toward the leading edge. The trailing
444 edge vortex shedding frequency identified in the dotted area is illustrated in
445 Figure12 at $U_\infty > 8$ m/s. Due to a large displacement of the LSB toward
446 the leading edge and the early establishment of turbulent boundary layer in

447 a relatively strong adverse pressure gradient region, the turbulent boundary
 448 layer tends to detach at the trailing edge for the highest velocities, although
 449 the wall friction increases. This phenomenon had been investigated numeri-
 450 cally previously, in [11]; in this study, an abrupt transition to turbulent flow
 451 caused by a leading edge LSB was associated with the sudden generation of a
 452 vortex at the trailing edge, caused by detachment of the turbulent boundary
 453 layer (see also Figure 12 at $U_\infty > 8\text{m/s}$, in orange). Finally, the additional
 454 frequencies around 400Hz for $4.5\text{m/s} < U_\infty < 8\text{m/s}$ are natural vibrations of
 455 the hydrofoil excited by LSB vortex shedding, which are not investigated in
 456 this paper.

457

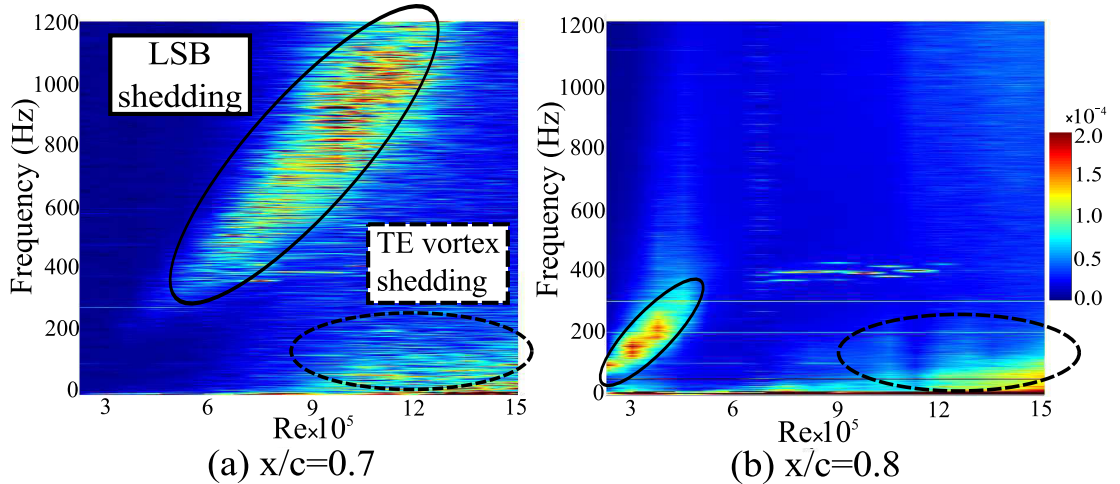


Figure 11: Experimental frequency spectra of wall pressure at (a) $x/c=0.7$ and (b) $x/c=0.8$ as function of Reynolds number, $\alpha = 4^\circ$.

458 Figure 13 compares the local wall pressure coefficients measured exper-
 459 imentally to those obtained with DNS at $Re = 450,000$, $U_\infty = 3\text{m/s}$, for

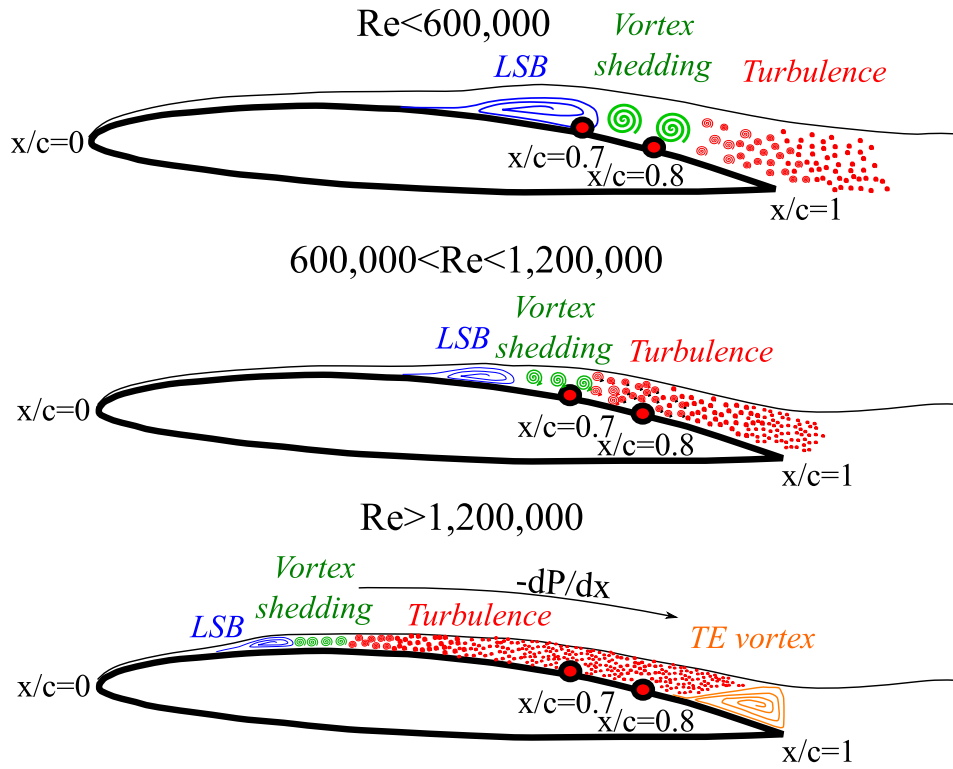


Figure 12: Evolution of LSB dynamics with the Reynolds number. TE=trailing edge.

460 $x/c = 0.7$, $x/c = 0.8$ and $x/c = 0.9$. The full DNS is plotted in time, and
 461 adjusted temporally to be synchronized with the experimental signal. Over-
 462 all there is good agreement between the DNS and experiments, in terms
 463 of temporal behavior and amplitudes. In the transition region at $x/c = 0.7$
 464 (Figure 13 (a)), the flow is highlighted by the development of coherent struc-
 465 tures and the pressure fluctuations show a strong periodic and intermittent
 466 behavior for both DNS and experiments. The amplitudes and modulations
 467 are fully captured by the present computations. With the development of
 468 turbulence, the pressure signal shows smaller fluctuations with random be-

469 havior; however the signal is still periodic for $x/c = 0.8$. Near the trailing
470 edge, i.e. at $x/c = 0.9$, the fluctuations are more random with significantly
471 lower amplitudes, clearly demonstrating turbulent fluctuation.

472

473 In order to refine the comparison between the measured and predicted
474 wall pressures, a fast fourier transform was performed on the signals shown
475 in Figure 13. The results are shown in Figure 14. Again, there was good
476 agreement between DNS and measurements for all spectra. At $x/c = 0.7$,
477 DNS captures the main frequency peak of LSB vortex shedding, with good
478 agreement in both amplitude and frequency range. A secondary peak around
479 500Hz is also observed, resulting from intermittency. At higher frequencies,
480 there is a rapid decay in amplitude. At $x/c = 0.8$ and $x/c = 0.9$, the
481 main peak is still observed, but with a progressive reduction in amplitude,
482 as also observed in experiments. Moving closer to the trailing edge, an in-
483 crease in amplitude at higher frequencies is observed, due to development of
484 turbulence. Again, this matches the experimental data, demonstrating the
485 accuracy of the simulation.

486

487 An isosurface of λ_2 (introduced in [20]) is shown in Figure 15 for $0.6 <$
488 $x/c < 1$, colored with pressure coefficient contours. This figure illustrates a
489 correlation between the evolution of wall pressure, and the boundary layer
490 transition to turbulence. It shows where coherent structures start to form
491 downstream from the LSB, and where the transition to turbulence occurs.
492 Coherent structures associated with the development of TS waves appear
493 at $x/c = 0.65$, which is very close to the point of laminar separation at

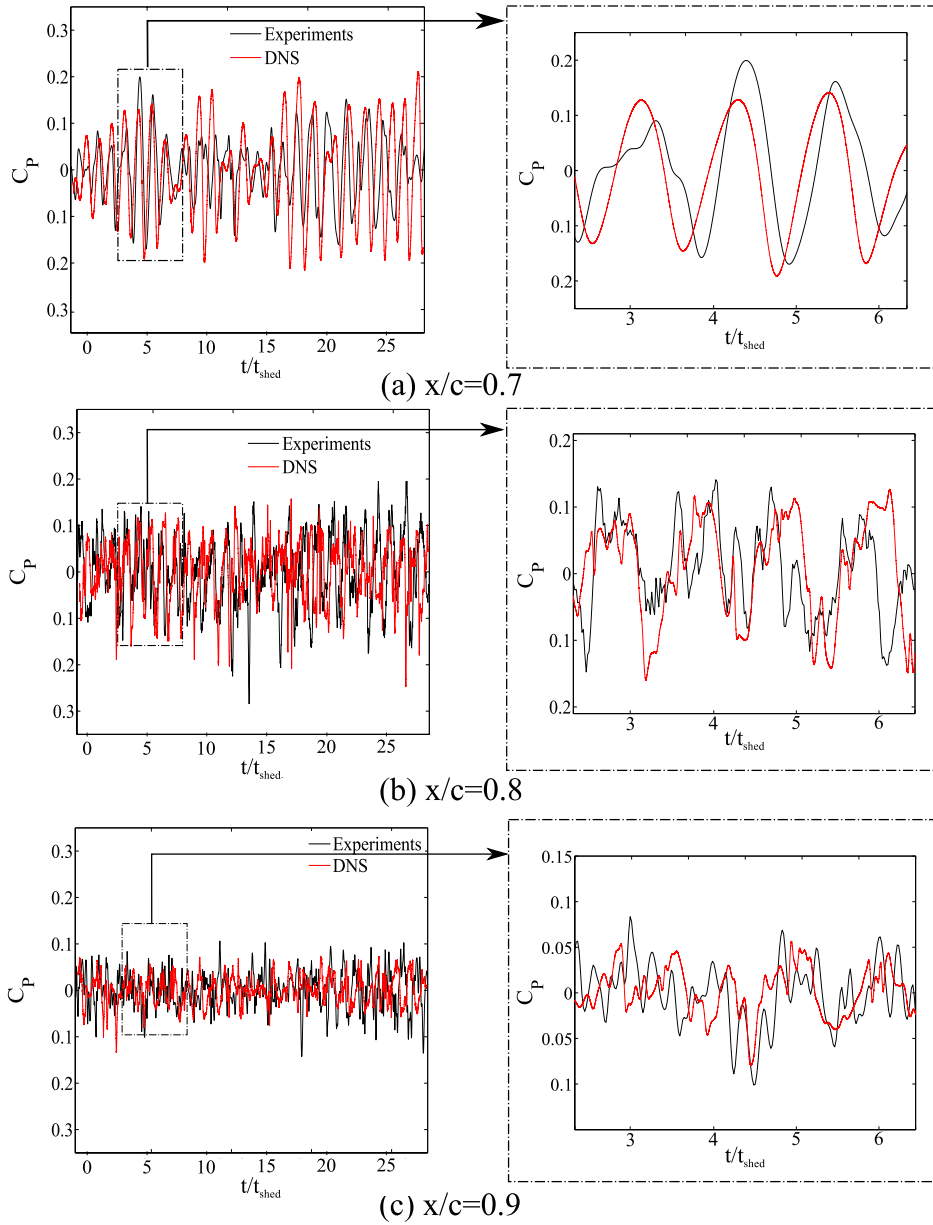
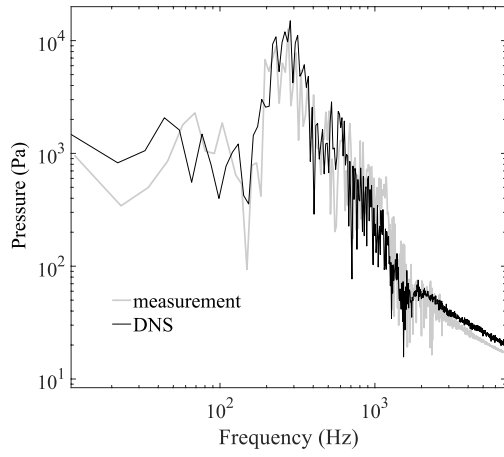
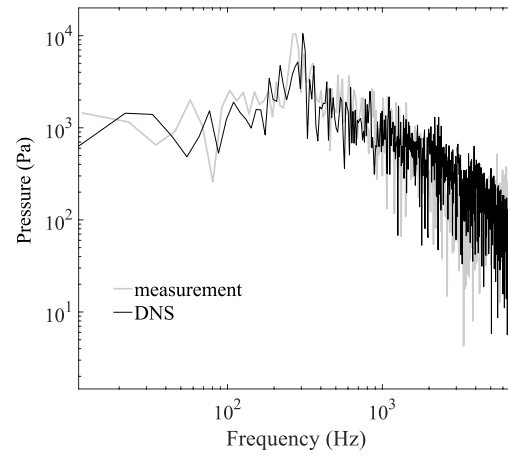


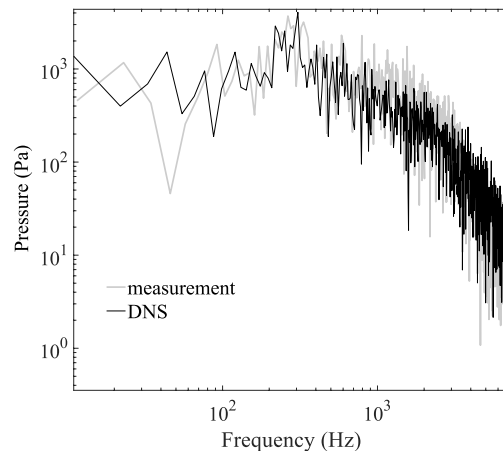
Figure 13: Comparison of computed and measured wall pressure coefficient, $Re = 450,000$, $U_\infty = 3\text{m/s}$



(a) $x/c = 0.7$



(b) $x/c = 0.8$



(c) $x/c = 0.9$

Figure 14: Spectral comparison of measured and DNS pressure signals for different chord-wise locations, $Re=450\,000$

494 $x/c = 0.62$, see Table 2. The dynamics remain approximately 2D until
 495 $x/c = 0.7$. This is consistent with figure 13 (a), which shows that wall pres-
 496 sure is fully periodic in this location. In the region $0.7 < x/c < 0.8$, the 2D
 497 vortex deforms and breaks down. Coherent structures are still present, in
 498 agreement with the periodicity in the pressure signal shown in Figure 13 (b).
 499 Subsequently, only turbulent structures are observed up to trailing edge.

While experiments allow a wide range of velocity conditions, they are limited

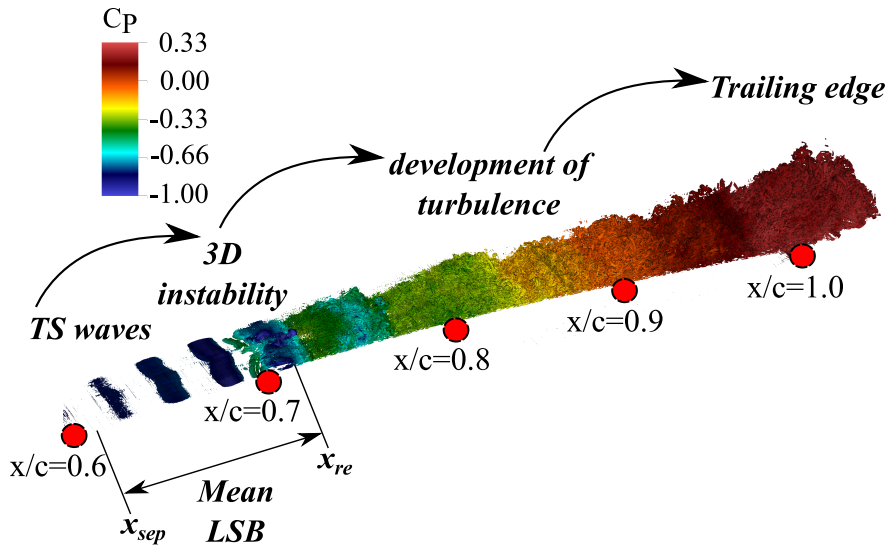


Figure 15: Coherent structures downstream from the LSB, isosurface of λ_2 colored with pressure coefficient, $Re = 450,000$

500

501 spatially to only three points placed in the transition region, and generally
 502 only one pressure transducer to record the bubble dynamic. In contrast, the
 503 DNS cannot be used to investigate a wide range of Reynolds numbers be-
 504 cause of the cost of a single computation, but can offer a complete spatial
 505 description of the flow. As such, a complete map of the wall pressure coef-
 506 ficients along the chord ($0.6 < x/c < 1$) over 25 periods is shown in Figure

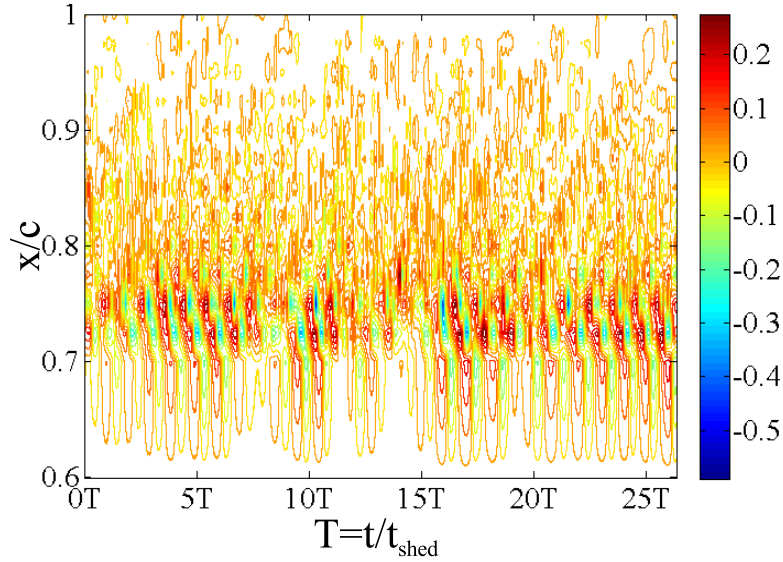


Figure 16: Time evolution of computed wall pressure coefficient fluctuations along the chord of the hydrofoil, $Re=450,000$

507 16. Periodic pressure fluctuations appear starting $x/c = 0.62$, i.e. near the
 508 laminar separation of LSB. For $0.7 < x/c < 0.75$, the pressure fluctuations
 509 increase in amplitude, after which they quickly lose their periodicity, reach-
 510 ing fully turbulent flow after $x/c = 0.85$, in agreement with the numerical
 511 observations in Figure 15.

512 4.3. Analysis of transition behavior: DNS at $Re=450,000$

513 Figure 17 shows the instantaneous velocity field and RMS of the spanwise
 514 velocity extracted from the mean flow. It is clear that the RMS increases in
 515 the unsteady region of the LSB, and is maximum near the turbulent reat-
 516 tachment. It remains high in the transition region, then decreases when
 517 turbulence is established. The instantaneous velocity field shows that the

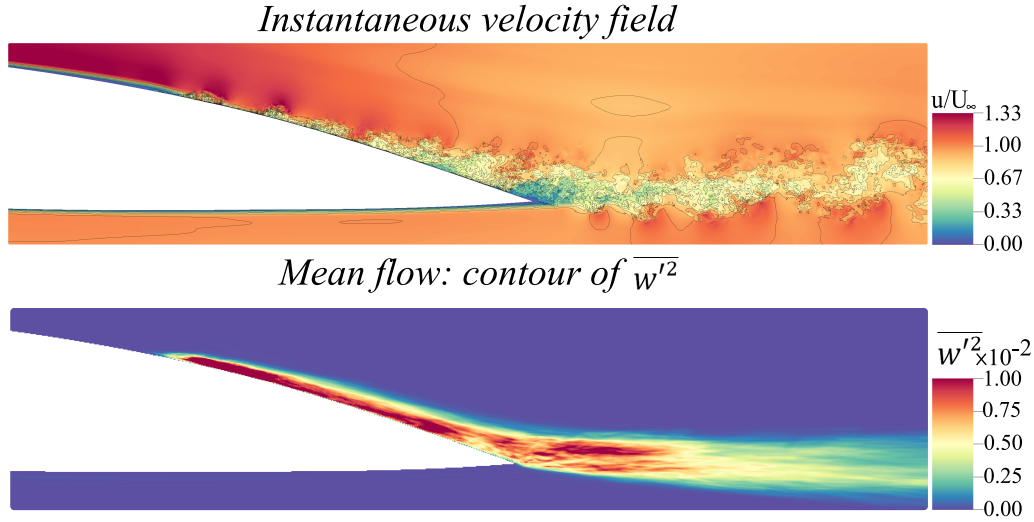


Figure 17: Evolution of unsteadiness downstream from the LSB, $Re=450,000$

518 suction side boundary layer increases in thickness with the development of
 519 turbulent boundary layer, which interacts with the pressure side boundary
 520 layer at the trailing edge to form a turbulent wake instability.

521 Figure 18 shows the spectra of V_x at three locations along the chord:
 522 $x/c = 0.7$, just downstream from the LSB; $x/c = 0.85$, between the transi-
 523 tional and turbulent regions; and $x/c = 1$, in the turbulent region. Velocities
 524 were recorded outside of the boundary layer. At $x/c = 0.7$, only the LSB
 525 vortex shedding frequency is observed on the spectra. At $x/c = 0.85$, this
 526 peak is still observed, and additionally a high amplitude is observed, cor-
 527 responding to the increased RMS shown in Figure 17. The development of
 528 turbulence also leads to the inception of higher frequency components. Fi-
 529 nally, at $x/c = 1$, the spectra shows a classical $-5/3$ slope resulting from the
 530 turbulent cascade.

531

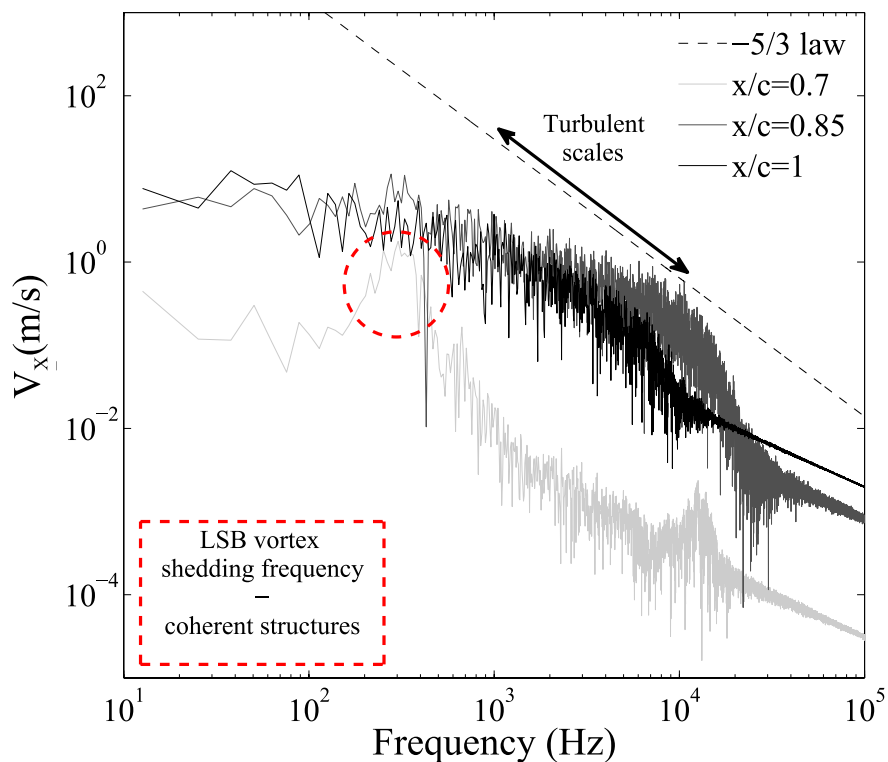


Figure 18: Spectra of V_x for three chordwise locations, $Re=450,000$

532 Finally, the transition mechanism for $Re = 450000$ is detailed in Fig-
 533 ure 19, which shows the isosurfaces of λ_2 colored with velocity and pressure
 534 coefficient contours. The top and bottom subfigures were produced using
 535 different values of λ_2 in order to highlight the different mechanisms: devel-
 536 opment of TS waves for higher λ_2 , and development of hairpin structures and
 537 turbulence downstream from the LSB for lower λ_2 . First, it can be observed
 538 on Figure 19(a) that the flow exhibits a typical H-type or K-type transition,
 539 as shown for the case of a flat plate with forcing by [35]. The distinction

540 between these two types of transition cannot be identified in this paper, as
541 only one Λ shape structure was captured spanwise, so it is not possible to
542 determine whether it is aligned (K-type) or staggered (H-type). The top
543 view of Figure 19 shows that TS waves appear downstream from the LSB,
544 and progressively deform with the inception of a 3D instability known as an
545 elliptic primary instability ([28]). The development of this instability leads
546 to the formation of a Λ -shaped structure, also known as a "hairpin" struc-
547 ture, whose breakdown leads to development of turbulent flow. It should be
548 noted that the Reynolds number Re_x at which this transition takes place
549 is comparable to that identified in [35], albeit advanced somewhat due to
550 the angle of attack and the curvature of the hydrofoil: as an example, the
551 TS waves start at $Re = 310000$, compared to $Re = 360000$ for [35]. The
552 velocity field in Figure 19(b) shows that the breakdown of Λ structures is
553 due to development of secondary instabilities, which progressively lead to
554 turbulence. The investigation of the pressure field in Figure 19(c) shows that
555 the pressure is globally maintained (dark blue) during development of the
556 hairpin structure. This means that the vortex convects along the chord with
557 a quasi-constant angular velocity, i.e. it extends the pressure plateau from
558 the LSB region. In the breakdown region, mixing leads to an increase in
559 pressure fluctuations, characterized by more random behavior. In the tur-
560 bulent region, the pressure increases almost linearly up to the trailing edge.

561

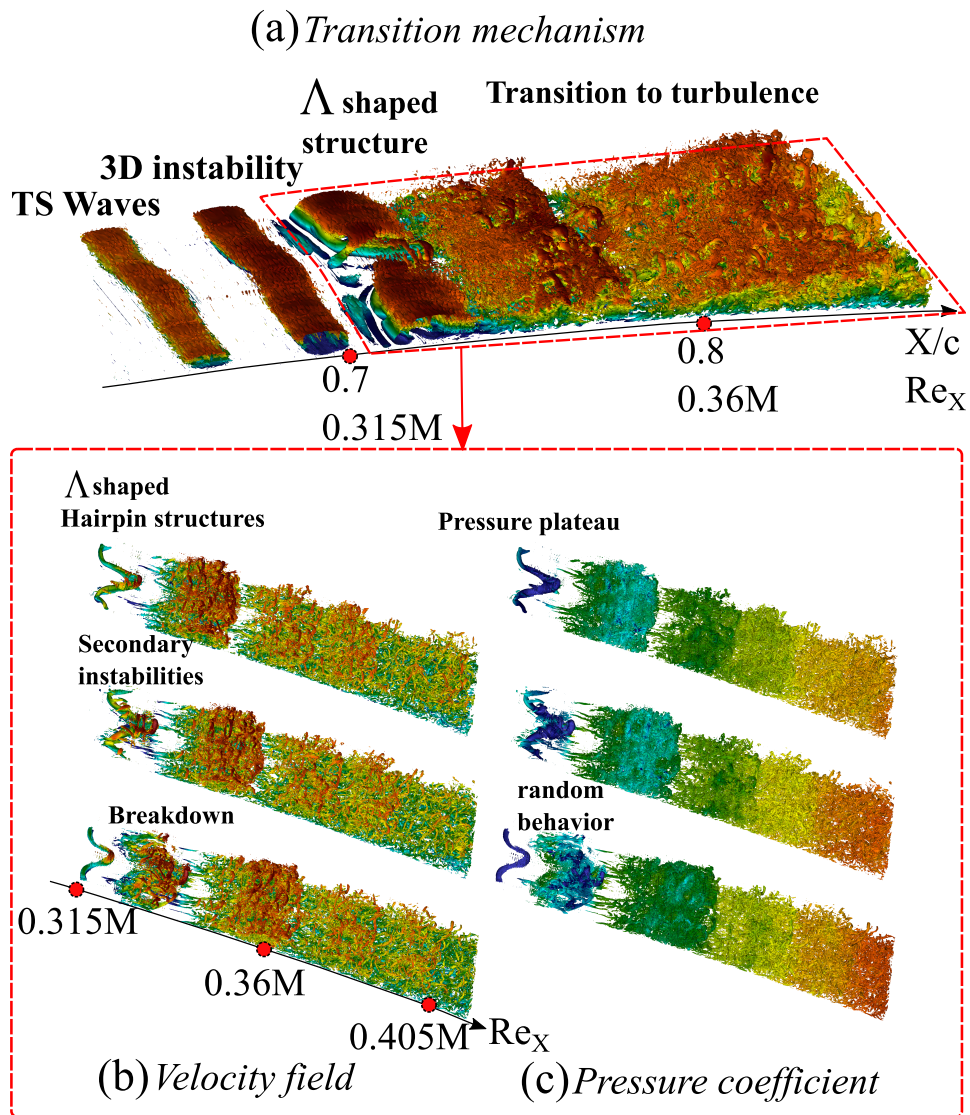


Figure 19: Time evolution of computed wall pressure coefficient fluctuations along the chord of the hydrofoil, isosurfaces of λ_2 colored with velocity contours (top and bottom left) and pressure coefficients contours (bottom right).

562 5. Conclusion

563 In this paper, the laminar to turbulent transition and the resulting wall
564 pressure fluctuations were analyzed on a laminar NACA66 propeller section.
565 Despite the moderate Reynolds number investigated ($Re = 450,000$), DNS
566 resolution was successfully obtained by using a simplified fluid domain, which
567 considered the near wall region by imposing RANS velocity profiles at the
568 boundaries. The results were compared with wall pressure measurements
569 performed in a hydrodynamic tunnel.

570 The DNS correctly reproduced the velocity field as found from transitional
571 RANS calculations, allowing the main characteristics of the LSB to be cap-
572 tured. Experimental investigations of wall pressure fluctuations for a wide
573 range of Reynolds numbers ($225,000 < Re < 1,500,000$) at $\alpha = 4^\circ$ showed
574 that the frequency of vortex shedding downstream from the LSB increases
575 linearly with increasing Reynolds number. Further, the fluctuations move
576 progressively from $x/c = 0.8$ to $x/c = 0.7$, which is associated with a de-
577 crease of the LSB length and its shift toward the leading edge. The DNS
578 results for wall pressure fluctuations at $Re = 450,000$ showed good agree-
579 ment with experiment throughout the different stages, from development of
580 the LSB, through the transition process, up to fully turbulent flow.

581 Following this validation of the DNS, the interaction between boundary layer
582 flow and the evolution of wall pressure fluctuations was investigated. It was
583 observed that the flow exhibit a classical H-type or K-type transition to tur-
584 bulence, highlighted by the inception of 2D TS waves, which deform to hair-
585 pin structures due to a 3D instability. A secondary instability subsequently
586 causes degradation of the hairpin structures, and the flow transitions quickly

587 to turbulence. The wall pressures were observed to respond to these different
588 stages of transition:

- 589 • from the inception of TS waves at $x/c = 0.65$ to the development of
590 hairpin structures at $x/c = 0.72$, the wall pressures display periodic
591 intermittent behavior with one main period that corresponds to LSB
592 vortex shedding.
- 593 • The breakdown around $x/c = 0.75$ has a mixing effect associated with
594 maximum amplitude of wall pressure fluctuations, which subsequently
595 decrease quickly for $0.75 < x/c < 0.8$. Periodic pressure fluctuations
596 are still observed, but with a greater degree of randomness due to
597 multi-scaled structures passing through the local surface.
- 598 • In the region of fully developed turbulence ($x/c > 0.85$) the pressure
599 signal reveals random fluctuations of lower amplitude.

600 It should be noted that because of the complex transitional flow captured,
601 boundary layer flow cannot be fully characterized due to certain numerical
602 effects. From laminar separation up to the inception of TS waves, typical
603 boundary layer flow is reproduced, suggesting the DNS is free of numerical
604 effects, mainly because it is a 2D process. As shown in [33], LSB shedding
605 LSB depends mainly on the boundary layer characteristics at laminar sepa-
606 ration, which appear to be correctly predicted by the DNS, as indicated by
607 the comparison of wall pressures with experiments. On the other hand, in
608 the transition region, where secondary instabilities play an important role
609 in the destabilization of the LSB, the numerical setup can strongly influence
610 the development and breakdown of 3D structures. In particular, because of

611 the reduced span used in the present simulation, it captures only one coher-
612 ent hairpin structure in the spanwise direction, so the flow may be forced
613 and hence the actual wavelength is probably not fully accurate. This aspect
614 will be investigated in future work by extending the DNS domain size in the
615 normal and spanwise directions. The present setup is also currently used to
616 study fluid structure interaction in transitional flows.

617

618 Acknowledgements

619 This work was performed using HPC resources of GENCI/IDRIS (Grant
620 2016-[100631]) at Orsay, France on the IBM Blue Gene/Q (Turing). Flow
621 visualizations were made using the open-source software VisIt [6].

622 References

- 623 [1] Astolfi, J.-A., Dorange, P., Billard, J.-Y., Tomas, I. C., 2000. An ex-
624 perimental investigation of cavitation inception and development on a
625 two-dimensional eppler hydrofoil. *Journal of Fluids Engineering* 122 (1),
626 164–173.
- 627 [2] Baltazar, M., Rijpkema, D., Falco de Campos, J., 2017. On the use of the
628 $\gamma - re_\theta$ transition model for the prediction of the propeller performance
629 at model scale. In: *Proceeding of the Fifth International Symposium on*
630 *Marine Propulsors*, 12nd - 15th June, Helsinki - Finland.
- 631 [3] Burgmann, S., Dannemann, J., Schröder, W., 2008. Time-resolved and
632 volumetric piv measurements of a transitional separation bubble on an
633 sd7003 airfoil. *Experiments in Fluids* 44 (4), 609–622.

- 634 [4] Burgmann, S., Schröder, W., 2008. Investigation of the vortex induced
635 unsteadiness of a separation bubble via time-resolved and scanning piv
636 measurements. *Experiments in fluids* 45 (4), 675.
- 637 [5] CARLTON, J., 1994. *Marine propellers and propulsion*. Butterworths-
638 Heinemann.
- 639 [6] Childs, H., Brugger, E., Whitlock, B., Meredith, J., Ahern, S., Pugmire,
640 D., Biagas, K., Miller, M., Harrison, C., Weber, G. H., Krishnan, H., Fo-
641 ggal, T., Sanderson, A., Garth, C., Bethel, E. W., Camp, D., Rübél, O.,
642 Durant, M., Favre, J. M., Navrátil, P., Oct 2012. VisIt: An End-User
643 Tool For Visualizing and Analyzing Very Large Data. In: *High Per-
644 formance Visualization—Enabling Extreme-Scale Scientific Insight*. pp.
645 357–372.
- 646 [7] Davidson, L., 2011. *Fluid mechanics, turbulent flow and turbulence
647 modeling*. Chalmers University of Technology, Goteborg, Sweden (Nov
648 2011).
- 649 [8] Delafin, P. L., Deniset, F., Astolfi, J.-A., 2014. Effect of the laminar
650 separation bubble induced transition on the hydrodynamic performance
651 of a hydrofoil. *European Journal of Mechanics-B/Fluids* 46, 190–200.
- 652 [9] Demir, H., Genç, M. S., 2017. An experimental investigation of lami-
653 nar separation bubble formation on flexible membrane wing. *European
654 Journal of Mechanics-B/Fluids* 65, 326–338.
- 655 [10] Deville, M., Fischer, P., Mund, E., 2002. *High-Order methods for in-
656 compressible fluid flow*. Cambridge University Press.

- 657 [11] Ducoin, A., Astolfi, J. A., Deniset, F., Sigrist, J. F., 2009. Computa-
658 tional and experimental investigation of flow over a transient pitching
659 hydrofoil. *Eur. J. Mech. B/Fluids* 28, 728–743.
- 660 [12] Ducoin, A., Astolfi, J. A., Gobert, M.-L., 2012. An experimental study
661 of boundary-layer transition induced vibrations on a hydrofoil. *J. Fluids*
662 *Struct.* 32, 37–51.
- 663 [13] Ducoin, A., Loiseau, J.-C., Robinet, J.-C., 2016. Numerical investigation
664 of the interaction between laminar to turbulent transition and the wake
665 of an airfoil. *European Journal of Mechanics-B/Fluids* 57, 231–248.
- 666 [14] Eca, L., Lopes, R., Vaz, G., Baltazar, J., Rijpkema, D. ., 2016. Validat-
667 ion exercises of mathematical models for the prediction of transitional
668 flows. In: *In: Proceedings of 31st Symposium on Naval Hydrodynamics,*
669 *11th-16th September, Berkeley.*
- 670 [15] Fischer, P., Kruse, J., Mullen, J., Tufo, H., Lottes, J., Kerkemeier, S.,
671 2008. Nek5000—open source spectral element cfd solver. Argonne Na-
672 tional Laboratory, Mathematics and Computer Science Division, Ar-
673 gonne, IL, see <https://nek5000.mcs.anl.gov/index.php/MainPage>.
- 674 [16] Gaster, M., 1966. The structure and behaviour of laminar separation
675 bubbles. *AGARD CP* 4, 813–854.
- 676 [17] Genç, M. S., Karasu, İ., Açikel, H. H., 2012. An experimental study
677 on aerodynamics of naca2415 aerofoil at low re numbers. *Experimental*
678 *Thermal and Fluid Science* 39, 252–264.

- 679 [18] Hinze, J., 1975. Turbulence (2nd edn). New York: McGraw-Gill, 223–
680 225.
- 681 [19] Hosseini, S. M., Vinuesa, R., Schlatter, P., Hanifi, A., Henningson, D. S.,
682 2016. Direct numerical simulation of the flow around a wing section
683 at moderate reynolds number. International Journal of Heat and Fluid
684 Flow 61, 117–128.
- 685 [20] Jeong, J., Hussain, F., 1995. On the identification of a vortex. Journal
686 of fluid mechanics 285, 69–94.
- 687 [21] Jones, L. E., Sandberg, R. D., Sandham, N. D., 2008. Direct numerical
688 simulations of forced and unforced separation bubbles on an airfoil at
689 incidence. J. Fluid Mech. 602, 175.
- 690 [22] Karasu, I., Genç, M., Açikel, H., 2013. Numerical study on low reynolds
691 number flows over an aerofoil. J. Appl. Mech. Eng 2, 131.
- 692 [23] Karman, T. V., 1937. The fundamentals of the statistical theory of tur-
693 bulence. Journal of the Aeronautical Sciences 4 (4), 131–138.
- 694 [24] Karniadakis, G., Sherwin, S., 2005. Spectral/hp element methods for
695 computational fluid dynamics. Oxford science publications.
- 696 [25] Kerkemeier, S. G., 2010. Direct numerical simulation of combustion on
697 petascale platforms. Ph.D. thesis, ETH Zurich.
- 698 [26] Koca, K., Genç, M. S., Açikel, H. H., Çağdaş, M., Bodur, T. M., et al.,
699 2018. Identification of flow phenomena over naca 4412 wind turbine

- 700 airfoil at low reynolds numbers and role of laminar separation bubble
701 on flow evolution. *Energy* 144 (C), 750–764.
- 702 [27] Leroux, J. B., Coutier-Delgosha, O., Astolfi, J. A., 2005. A joint exper-
703 imental and numerical study of mechanisms associated to instability of
704 partial cavitation on two-dimensional hydrofoil. *Phys. Fluids* 17, 052101.
- 705 [28] Marxen, O., Lang, M., Rist, U., 2013. Vortex formation and vortex
706 breakup in a laminar separation bubble. *J. Fluid Mech.* 728, 58–90.
- 707 [29] Nati, A., De Kat, R., Scarano, F., Van Oudheusden, B., 2015. Dynamic
708 pitching effect on a laminar separation bubble. *Experiments in Fluids*
709 56 (9), 1–17.
- 710 [30] Olson, D. A., Katz, A. W., Naguib, A. M., Koochesfahani, M. M.,
711 Rizzetta, D. P., Visbal, M. R., 2013. On the challenges in experimental
712 characterization of flow separation over airfoils at low reynolds number.
713 *Experiments in fluids* 54 (2), 1–11.
- 714 [31] Park, S. K., Miller, K. W., 1988. Random number generators: good ones
715 are hard to find. *Communications of the ACM* 31 (10), 1192–1201.
- 716 [32] Patera, A., 1984. A spectral element method for fluid dynamics: laminar
717 flow in a channel expansion. *J. Comput. Phys.* 54, 468–488.
- 718 [33] Pauley, L. L., Moin, P., Reynolds, W. C., 1990. The structure of two-
719 dimensional separation. *J. Fluid Mech.* 220, 397–411.
- 720 [34] Reverberi, A., Lloyd, T., Vaz, G., 2016. Towards cavitation modelling

- 721 accounting for transition effects. proceeding of the 19th "Numerical Tow-
722 ing Tank Symposium" (NuTTS'16).
- 723 [35] Sayadi, T., Hamman, C. W., Moin, P., 2013. Direct numerical simula-
724 tion of complete h-type and k-type transitions with implications for the
725 dynamics of turbulent boundary layers. *Journal of Fluid Mechanics* 724,
726 480–509.
- 727 [36] Tufo, H. M., Fischer, P. F., 1999. Terascale spectral element algorithms
728 and implementations. In *Proceedings of the ACM/IEEE SC99 Confer-
729 ence on High Performance Networking and Computing*, Portland, U.S.A.
- 730 [37] Tufo, H. M., Fischer, P. F., 2001. Fast parallel direct solvers for coarse
731 grid problems. *J. Parallel Distrib. Comput.* 61 (2), 151–177.
- 732 [38] Uranga, A., Persson, P.-O., Drela, M., Peraire, J., 2011. Implicit large
733 eddy simulation of transition to turbulence at low reynolds numbers
734 using a discontinuous Galerkin method. *International Journal for Nu-
735 merical Methods in Engineering* 87 (1-5), 232–261.
- 736 [39] Visbal, M. R., Gordnier, R. E., Galbraith, M. C., 2009. High-fidelity
737 simulations of moving and flexible airfoils at low reynolds numbers. *Ex-
738 periments in Fluids* 46 (5), 903–922.
- 739 [40] Zhang, W., Hain, R., Kähler, C. J., 2008. Scanning piv investigation of
740 the laminar separation bubble on a sd7003 airfoil. *Experiments in Fluids*
741 45 (4), 725–743.
- 742 [41] Zhang, W., Samtaney, R., 2016. Assessment of spanwise domain size

743 effect on the transitional flow past an airfoil. *Computers & Fluids* 124,
744 39–53.